npj | Quantum Information

www.nature.com/npjqi

ARTICLE OPEN

Check for updates

Nuclear spin assisted magnetic field angle sensing

Ziwei Qiu[1,2], Uri Vool[1,3], Assaf Hamo[1] and Amir Yacoby[1,2]✉

Quantum sensing exploits the strong sensitivity of quantum systems to measure small external signals. The nitrogen-vacancy (NV) center in diamond is one of the most promising platforms for real-world quantum sensing applications, predominantly used as a magnetometer. However, its magnetic field sensitivity vanishes when a bias magnetic field acts perpendicular to the NV axis. Here, we introduce a different sensing strategy assisted by the nitrogen nuclear spin that uses the entanglement between the electron and nuclear spins to restore the magnetic field sensitivity. This, in turn, allows us to detect small changes in the magnetic field angle relative to the NV axis. Furthermore, based on the same underlying principle, we show that the NV coupling strength to magnetic noise, and hence its coherence time, exhibits a strong asymmetric angle dependence. This allows us to uncover the directional properties of the local magnetic environment and to realize maximal decoupling from anisotropic noise.

npj Quantum Information (2021)7:39 ; https://doi.org/10.1038/s41534-021-00374-6

INTRODUCTION

Quantum sensing harnesses the coherence of well-controlled quantum systems to detect small signals with high sensitivity[1–3]. Typically, an external signal directly leads to a shift of the quantum sensor's energy levels. Ancillary sensors, which do not interact with the signal directly, can assist the main sensor by, for example, acting as a long-lived quantum memory[4–8] or providing error correction[9–14]. Solid state spins are promising platforms for quantum sensing techniques and applications, among which nitrogen-vacancy (NV) centers in diamond have received the most attention[2,15–17]. The electron spin associated with the negatively charged NV center has long coherence time even at room temperature and is capable of detecting a variety of signals with high sensitivity and nanoscale resolution. These include magnetic[18–20] and electric fields[21–28], temperature[29–32], and pressure[33–35].

For the NV to act as a magnetometer, a bias magnetic field along the NV axis is generally required to put the electron spin ($S = 1$) in the $|m_S = 0, \pm 1\rangle$ basis, such that the energy levels are first-order sensitive to magnetic field perturbations[2]. However, this method fails when the bias field turns toward the direction perpendicular to the NV axis, where the Zeeman interaction no longer induces energy shifts between the levels. To unlock the full potential under this unfavored condition, we introduce an entirely different sensing approach assisted by the ancillary ^{15}N nuclear spin. The essential principle is based on the sensitivity of the hyperfine interaction (between the electron and nuclear spins) to small magnetic signals. By monitoring the entanglement between the two spins using spin-echo sequences, we detect small changes in the magnetic field angle. Furthermore, similar to the hyperfine interaction, we show that the coupling between the electron spin and magnetic noise also sensitively depends on the bias field angle, which can be further employed to distinguish and characterize anisotropic noise in the environment. Our exploration extends the capabilities of the versatile sensing toolkit of the NV center, and this sensing strategy based on the interaction between the main sensor and ancillary sensor can be implemented on other quantum sensing platforms as well.

Our experiments were done under ambient conditions, as schematically depicted in Fig. 1a, b. The single-crystal diamond chip contains individually resolvable ^{15}NVs. A metal stripline fabricated on the diamond surface delivers microwave currents to manipulate the NV spin states. A cylindrical permanent magnet exerts a magnetic field at the NV and provides a coarse control of the field angle (θ_B), while a small DC current flowing in the stripline fine-tunes θ_B in the close vicinity of 90°. We define $\hat{z}$ to be the NV axis and $\hat{x}$ to be the bias magnetic field direction when it is exactly perpendicular (Fig. 1a).

The paper is structured as follows. We begin by analyzing the NV electron energy eigenstates as the magnetic field angle θ_B varies around 90°. In particular, we study how the angle modulates the electron spin operator expectation values $\langle \mathbf{S} \rangle$ at each state, and consequently affects its interaction with the ^{15}N nuclear spin. Next, we demonstrate magnetic field angle sensing by using spin-echo interferometry to measure the angle-dependent hyperfine interaction. Lastly, we show that the NV coherence exhibits an asymmetric angle dependence, which originates from anisotropic noise in the environment.

RESULTS

Electron spin eigenstate properties

The NV spin ground state Hamiltonian H_{gs} can be written as:

$$H_{gs} = H_e + H_n$$
$$H_e = D_{gs} S_z^2 + \gamma_B (B_x S_x + B_z S_z)$$
$$H_n = \mathbf{I} \cdot \mathbf{A} \cdot \mathbf{S} + \gamma_N (B_x I_x + B_z I_z),$$

where H_e and H_n denote the Hamiltonians associated with the electron spin ($S = 1$) and ^{15}N nuclear spin ($I = \frac{1}{2}$), respectively. $D_{gs} \approx 2.87$ GHz is the zero-field splitting, $\gamma_B \approx 2.87$ MHz/G is the electron spin gyromagnetic ratio, $\gamma_N \approx 0.4316$ kHz/G is the ^{15}N nuclear spin gyromagnetic ratio, and $\mathbf{A}$ is the hyperfine tensor with only diagonal elements: $A_{xx} = A_{yy} \approx 3.65$ MHz and $A_{zz} \approx 3.03$ MHz[36–38]. $S_{x,y,z}$ and $I_{x,y,z}$ are the spin-1 and spin-$\frac{1}{2}$ Pauli matrices, respectively. We applied the bias field $|B| > 60$ G, such that H_e always dominates over H_n (at any θ_B). The electron eigenstates, denoted by $|0, \pm\rangle$ throughout the paper, are thus mainly

[1]Department of Physics, Harvard University, Cambridge, MA, USA. [2]John A. Paulson School of Engineering and Applied Sciences, Harvard University, Cambridge, MA, USA. [3]John Harvard Distinguished Science Fellows Program, Harvard University, Cambridge, MA, USA. ✉email: yacoby@physics.harvard.edu

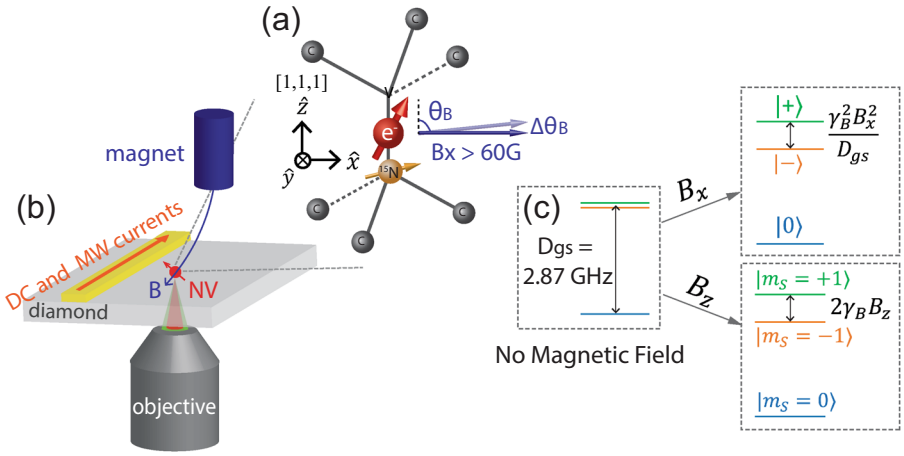

Fig. 1 Schematic of the NV center and experimental setup. a ^{15}NV in the presence of a bias magnetic field acting perpendicular to the NV symmetry axis. The coordinate system is depicted on the left. The bias magnetic field direction rotates in the XZ plane. θ_B is varied around 90° and $\Delta\theta_B$ is the signal to be detected. **b** A permanent magnet and DC currents in the metal stripline together control the magnetic field at the NV. **c** NV electron energy eigenstates under parallel (B_z) and perpendicular (B_x) magnetic fields.

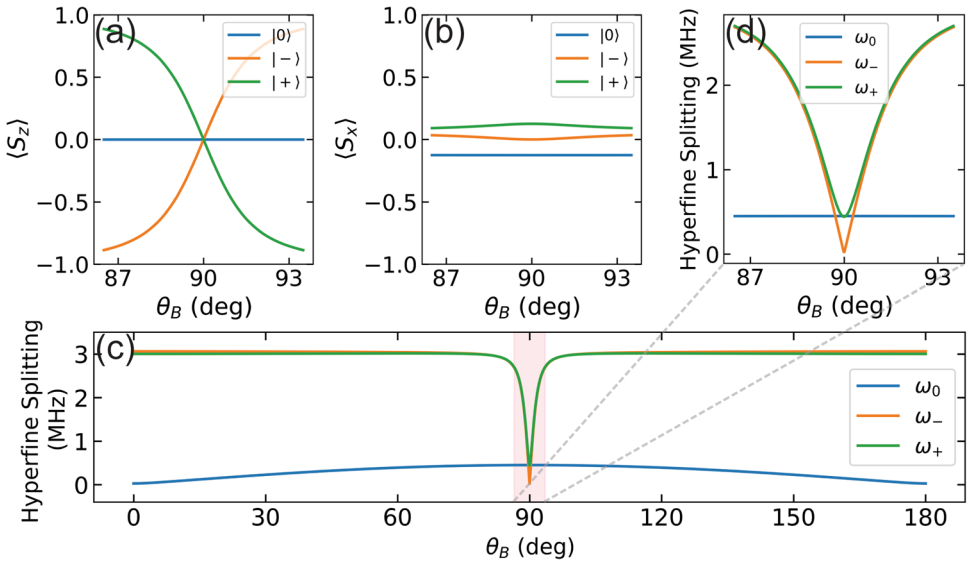

Fig. 2 NV electron spin eigenstate properties under a nearly perpendicular magnetic field. a, **b** Angle dependence of the electron spin operator expectation values $\langle \mathbf{S} \rangle$ at each state $|0, \pm\rangle$, calculated under $|B| = 65$ G. $\langle S_y \rangle = 0$ for all states, thus is not plotted. **c**, **d** Angle dependence of the nuclear spin sublevel splittings ω at each electron state. **c** zooms in on the red shaded area around 90° in (**d**). ω_-, the orange curve in (**d**), sharply increases with the off-angle $\Delta\theta_B$, serving as the key to our angle sensing approach.

determined by H_e, and H_n splits each state into two nuclear spin sublevels (see Supplementary Note 2B).

Under a bias magnetic field along $\hat{z}$ ($\theta_B = 0$), i.e., the conventional magnetometry condition, the electron eigenstates are $|m_S = 0, \pm 1\rangle$ (Fig. 1c). As the bias field direction rotates ($\theta_B \neq 0$), the eigenbasis changes. At $\theta_B = 90°$ ($B_z = 0$, $B_x > 0$), the eigenstates are as follows: $|0\rangle \approx |m_S = 0\rangle, |-\rangle = \frac{1}{\sqrt{2}}(|m_S = +1\rangle - |m_S = -1\rangle), |+\rangle \approx \frac{1}{\sqrt{2}}(|m_S = +1\rangle + |m_S = -1\rangle)$, and the states $|\pm\rangle$ split in energy by $\approx \frac{\gamma_B^2 B_x^2}{D_{gs}}$ (Fig. 1c). Under large B_x, $|m_S = 0\rangle$ and $\frac{1}{\sqrt{2}}(|m_S = +1\rangle + |m_S = -1\rangle)$ are slightly hybridized in composing $|0\rangle$ and $|+\rangle$, hence the approximate equality in the above expressions. This hybridization results in finite $\langle S_x \rangle$ values for $|0\rangle$ and $|+\rangle$: $\langle S_x \rangle_0 < 0, \langle S_x \rangle_+ > 0$ (see Supplementary Note 2A).

The states $|\pm\rangle$ are equal superpositions of $|m_S = \pm 1\rangle$ at $\theta_B = 90°$, hence $\langle S_z \rangle_\pm = 0$. However, as θ_B deviates from 90°, the $|m_S = \pm 1\rangle$ amplitudes are no longer equal. Due to the large zero-field splitting, the imbalance grows rapidly with the off-angle $\Delta\theta_B \equiv \theta_B - 90°$, and consequently, $\langle S_z \rangle_\pm$ acquire finite values (Fig. 2a). On the other hand, $\langle S_x \rangle$ barely changes (Fig. 2b). The change in $\langle S_z \rangle$ dramatically affects the electron spin interaction with the nuclear spin, thus providing a way to sense $\Delta\theta_B$.

Angle-dependent hyperfine interaction

A given electron state exerts effective hyperfine fields at the nuclear spin, determined by its spin operator expectation values. Specifically, the nuclear spin Hamiltonian is $H_n = A_{||} I_x \langle S_x \rangle_{|\psi_e\rangle} + A_\perp I_z \langle S_z \rangle_{|\psi_e\rangle} + \gamma_N (B_x I_x + B_z I_z)$, where $|\psi_e\rangle = |0, \pm\rangle$. H_n splits each electron state ($|0, \pm\rangle$) into two nuclear sublevels and the splitting energy ($\hbar\omega$) can be obtained by diagonalizing H_n. Figure 2c plots ω as a function of θ_B calculated under $|B| = 65$ G and Fig. 2d zooms in on a small angle range centered at 90°. The $|-\rangle$ state splitting (ω_-) is especially interesting: it grows linearly with $\Delta\theta_B$. The slope $\frac{d\omega}{d\theta_B}$, as we will see soon, directly determines the angle sensitivity.

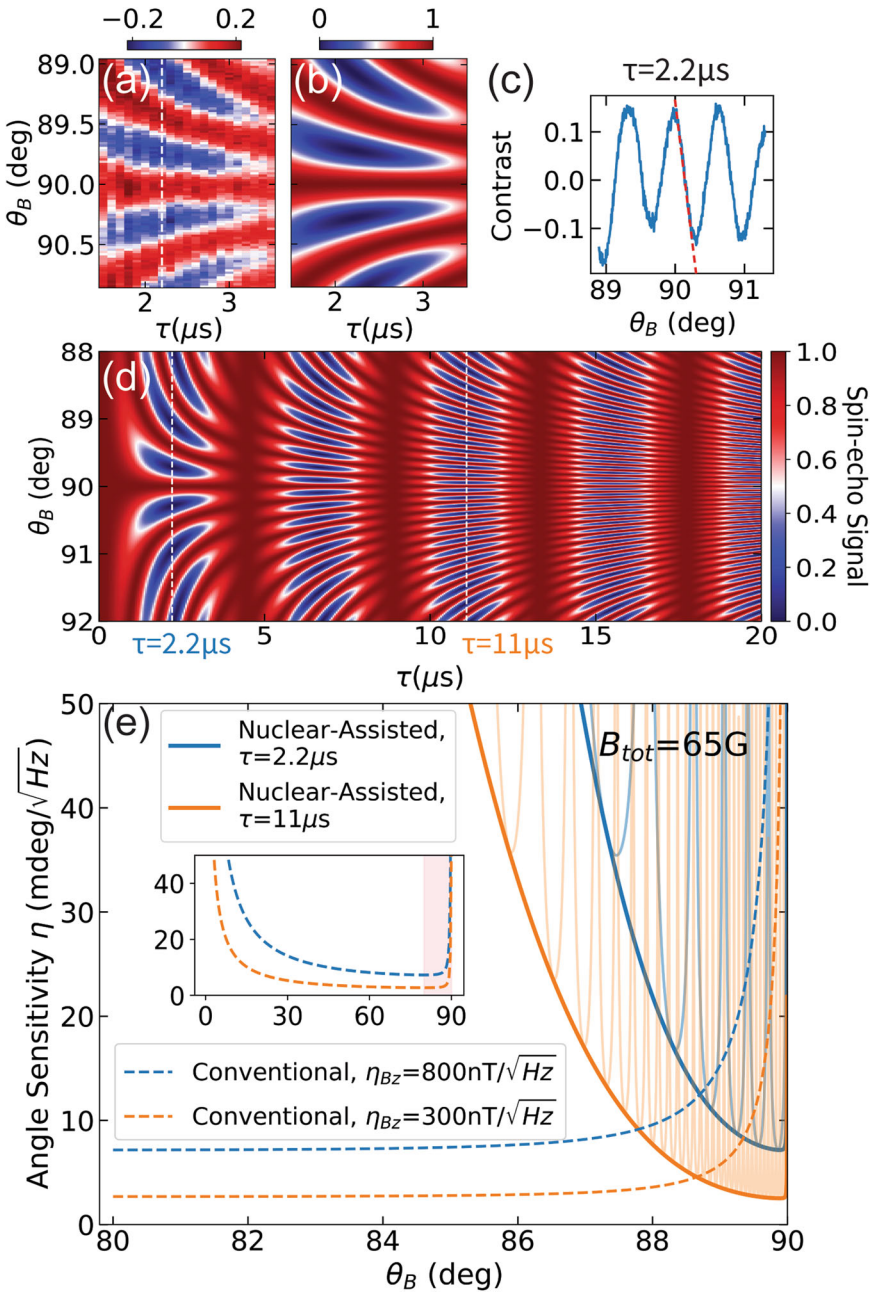

Fig. 3 Demonstration of nuclear spin assisted angle sensing using spin-echo interferometry. a Experimental and **b** theoretical spin-echo signal as a function of the free evolution time τ and θ_B under $|B| \approx 65$ G. The colorbar represents the fluorescence contrast in (**a**) and the spin-echo amplitude in (**b**). **c** The experimental spin-echo signal at fixed $\tau = 2.2$ μs (white dashed line in (**a**)). The red dashed line denotes the largest slope as θ_B varies. **d** Spin-echo calculation in broader θ_B and τ ranges, where the two white dashed lines mark the fixed τ times at which sensitivities are plotted in (**e**). **e** Comparison of angle sensitivities using the nuclear-assisted method (solid curves) in this work vs. conventional magnetometry (dashed curves) based on the electron Zeeman interaction. The nuclear-assisted sensitivities η oscillate with θ_B, as shown by the semi-transparent solid curves, while the thick curves sketch the envelopes η^*. They are compared with conventional approaches assuming two different B_z sensitivities ($300\frac{nT}{\sqrt{Hz}}$ and $800\frac{nT}{\sqrt{Hz}}$) under a parallel bias magnetic field. Inset: the conventional magnetometry sensitivity η_{con} in the full angle range.

Nuclear spin assisted angle sensing

We now demonstrate detection of small angle changes using the angle-sensitive hyperfine interaction. Either ω_- or ω_+ can be used, as they both change with θ_B. We choose to use ω_- since its angle dependence is steeper. To measure this quantity, we performed electron spin-echo interferometry, where the spin-echo signal is dramatically affected by the hyperfine splitting due to the electron-spin-echo-envelope-modulation (ESEEM) effect[39–42].

A typical spin-echo sequence is shown in Supplementary Fig. 3. The electron is first prepared in a superposition of $|0\rangle$ and $|-\rangle$, and then accumulates phase during the free evolution time τ between the two $\pi/2$ pulses. The π refocusing pulse decouples the fields at frequencies other than $1/\tau$.

The ESEEM effect occurs when the nuclear spin undergoes Larmor precession, with the frequency (ω_0 or ω_-) conditioned on the electron state ($|0\rangle$ or $|-\rangle$). Consequently, the electron and nuclear spins are periodically entangled and disentangled at a rate

determined by ω_0 and ω_-. The spin-echo amplitude measures the electron coherence, which is directly affected by its entanglement with the nuclear spin, hence exhibiting collapses and revivals. As ω_- is highly sensitive to θ_B, the spin-echo signal shows angle-dependent modulation patterns. A more detailed analysis is given in Supplementary Note 2C, where the spin-echo signal P obtains a simple expression: $P = 1 - |\hat{\omega}_0 \times \hat{\omega}_-|^2 \sin^2\left(\frac{\omega_0 \tau}{4}\right) \sin^2\left(\frac{\omega_- \tau}{4}\right)$.

We performed spin-echo experiments between $|0\rangle$ and $|-\rangle$ under $|B| \approx 65$ G, as θ_B varied between 89° and 91° (Fig. 3a). It shows good agreement with the above expression for P (Fig. 3b). At fixed $\tau = 2.2$ μs, the spin-echo signal can sensitively detect small angle changes at the largest slope (red dashed line in Fig. 3c). The corresponding sensitivity is $\sim 13 \frac{mdeg}{\sqrt{Hz}}$, provided the single NV fluorescence ~100 kcps and optical contrast ~15% in the experiment (see Supplementary Note 2D). To get an overall picture, Fig. 3d expands on Fig. 3b, showing the spin-echo signal P in broader θ_B and τ ranges.

Taking the derivative of P with respect to θ_B, we obtain an analytical expression of the angle sensitivity η (see Supplementary Note 2D):

$$\eta = \frac{\eta^*}{\left|\sin^2\left(\frac{\omega_0 \tau}{4}\right) \cdot \sin\left(\frac{\omega_- \tau}{2}\right)\right|} \quad (1)$$

$$\eta^* \equiv \frac{4}{\gamma_\theta C \sqrt{FT_r \tau}} \cdot \frac{t_{ini} + \tau}{\tau}, \quad (2)$$

where F represents the NV fluorescence, C the optical contrast of different spin states, t_{ini} the spin initialization time and T_r the spin state readout time. $\gamma_\theta \equiv \frac{d\omega_-}{d\theta_B}$ denotes the slope of the angle-dependent hyperfine interaction (Fig. 2d). Note that γ_θ is playing an analogous role as the gyromagnetic ratio in conventional magnetometry. The denominator in Eq. (1) causes modulation in τ, i.e. the angle sensitivity is periodically lost and regained at different τ times (Fig. 3d), and η^* in Eq. (2) is the modulation envelope. To optimize the sensitivity, we need to pick τ that maximizes $\left|\sin^2\left(\frac{\omega_0 \tau}{4}\right) \cdot \sin\left(\frac{\omega_- \tau}{2}\right)\right|$. As examples, sensitivities were evaluated at $\tau = 2.2$ μs and 11 μs and plotted in Fig. 3e, represented by the blue and orange solid curves, respectively.

On the other hand, conventional magnetometry also detects magnetic field angle changes via the electron Zeeman interaction. Its angle sensitivity is proportional to the static magnetic field sensitivity along $\hat{z}$: $\eta_{con} = \frac{\eta_{Bz}}{|B| \sin \theta_B}$. With a parallel bias magnetic field, η_{Bz} is typically between tens of $\frac{nT}{\sqrt{Hz}}$ and a few $\frac{\mu T}{\sqrt{Hz}}$ depending on experimental parameters[15,16], and η_{Bz} decreases as the bias field turns toward a perpendicular direction (see Supplementary Note 2E). Figure 3e plots η_{con} as a function of θ_B assuming η_{Bz} is originally 300 or 800 $\frac{nT}{\sqrt{Hz}}$ under a parallel bias field.

As illustrated in Fig. 3e, our nuclear-assisted approach and conventional magnetometry work in complimentary regimes. The conventional method works well until θ_B approaches 90° (Fig. 3e inset), when $\frac{\gamma_B^2 B_x^2}{D_{gs}} \gtrsim 2\gamma_B B_z$ so the electron eigenbasis changes from $|m_S = 0, \pm 1\rangle$ to $|0, \pm\rangle$, and after that the nuclear-assisted approach takes over. The sensitivities of both methods are limited by low-frequency noise, up to different effective coupling constants (see Supplementary Note 2E).

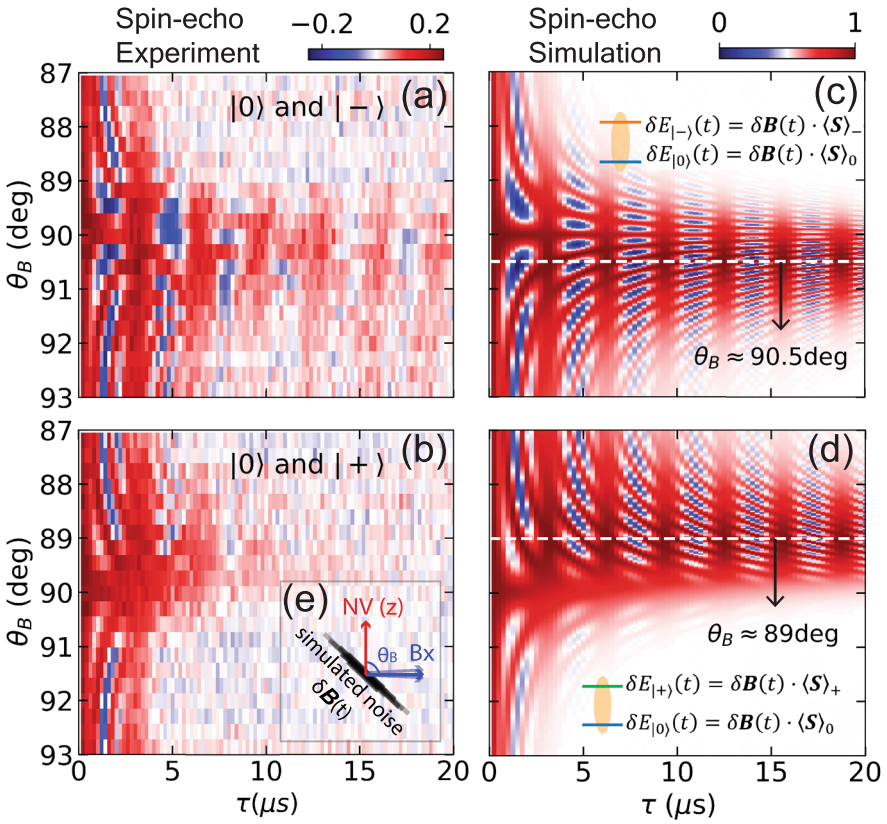

Fig. 4 Asymmetric angle dependence of the NV coherence time. a, b Spin-echo experiments between $|0\rangle$ and $|\mp\rangle$ as θ_B varies under $|B| \approx 93$ G. Colorbar represents the fluorescence contrast. The asymmetry between $\theta_B < 90°$ and $\theta_B > 90°$ originates from local anisotropic magnetic field noise in the sample. **c, d** Simulated spin-echo signals with a magnetic field noise acting along a direction at −45°/+135° from the $+\hat{x}$ axis, as depicted in (**e**). The white dashed lines mark the optimal angles at which the noise coupling is maximally suppressed. Colorbar represents the spin-echo amplitude.

Detection of anisotropic noise

The NV couples to magnetic field noise through its electron spin operators. Similar to the hyperfine interaction, the noise coupling strength, and hence the spin coherence, also exhibits strong angle dependence. We show that this provides a useful way to distinguish and characterize anisotropic noise.

Magnetic field noise $\delta\mathbf{B}(t)$ induces transition energy fluctuations: $\delta E_{\pm,0}(t) = \delta\mathbf{B}(t)\cdot(\langle\mathbf{S}\rangle_{\pm} - \langle\mathbf{S}\rangle_0)$, degrading the coherence between the states $|0\rangle$ and $|\pm\rangle$. It can be shown that the coherence is affected by the variance of the fluctuation $\langle\delta E^2\rangle$ (see Supplementary Note 3A). Recalling $\langle S_z\rangle$ ($\langle S_x\rangle$) in Fig. 2a, b, we get:

$$\langle\delta E^2_{-0}\rangle = \langle\delta B_x^2\rangle\langle S_x\rangle_0^2 + \langle\delta B_z^2\rangle\langle S_z\rangle_-^2 - 2\langle\delta B_x\delta B_z\rangle\langle S_x\rangle_0\langle S_z\rangle_- \quad (3)$$

$$\langle\delta E^2_{+0}\rangle = 4\langle\delta B_x^2\rangle\langle S_x\rangle_0^2 + \langle\delta B_z^2\rangle\langle S_z\rangle_+^2 - 4\langle\delta B_x\delta B_z\rangle\langle S_x\rangle_0\langle S_z\rangle_+ \quad (4)$$

The last terms in Eqs. (3) and (4) suggest the coherence is sensitive to the correlation between δB_x and δB_z, which is non-zero for anisotropic noise. Since $\langle S_z\rangle_{\pm}$ is an odd function of $\Delta\theta_B$, while $\langle S_x\rangle_0$ an even function, depending on the sign of $\langle\delta B_x\delta B_z\rangle$, the coherence is longer on one side than the other around $\theta_B = 90°$, and the states $|\pm\rangle$ show opposite asymmetry. If the noise is isotropic, i.e., $\langle\delta B_x\delta B_z\rangle = 0$, the coherence is then symmetric around 90°. Therefore, by examining the angle dependence of the coherence time, we can distinguish the anisotropic noise and further characterize its direction based on the asymmetry. This directional information, on the other hand, cannot be obtained under a parallel bias magnetic field ($\theta_B \approx 0°$), where the NV only couples to the $\hat{z}$ component of the noise.

The coherence asymmetry observed in our experiment (Fig. 4a, b) indicates that the noise coupled to the NV is anisotropic. We argue in Supplementary Note 3B that this is likely due to the dipolar interaction with a few nearby randomly-flipping spins (such as P1 centers or ^{13}C nuclear spins). To further illustrate this effect, we performed spin-echo simulation under a fully anisotropic noise, where the noise only fluctuates along a straight line at −45°/+135° relative to $+\hat{x}$ (Fig. 4e), such that $\delta B_x(t) + \delta B_z(t) = 0$. Under this condition, there exist optimal angles at which the noise coupling is maximally suppressed (white dashed lines in Fig. 4c, d).

DISCUSSION

While conventional NV magnetometry fails when the bias magnetic field orients perpendicular to the NV axis, here we demonstrated a method which uses the electron eigenbasis change for sensing. The achieved sensitivity ($\eta \approx 13\frac{mdeg}{\sqrt{Hz}}$) can be further improved by using cleaner diamond samples with less noise (e.g., by using ^{12}C enriched diamonds[43] or chemical termination to reduce surface spins[44]), increasing photon collection efficiency (e.g. by fabricating microlens[45–49] or pillars[50–54]) or using NV ensembles[55–57]. For example, as the sensitivity is improved by the square root of the number of NVs, a typical ensemble density of $10^{12}/cm^2$ can achieve $\eta < 0.3\frac{mdeg}{\sqrt{Hz}}$. Our work expands the already remarkable sensing versatility of the NV center. One example of the use of angle sensing is to allow precise tuning of a perpendicular magnetic field to the NV axis for electric field sensing[21–24,27,28].

Our sensing strategy relies on measuring the interaction with an ancillary sensor. Implementing this idea to other quantum sensing platforms requires two key ingredients. First, the angle-dependent hyperfine interaction is due to the NV eigenbasis change, which occurs when $\frac{\gamma_B^2 B_x^2}{D_{gs}} \sim \gamma_B B_z$. At $\theta_B \approx 90°$, this condition becomes $\frac{\gamma_B^2|B|^2}{D_{gs}} \sim \gamma_B|B|\sin\Delta\theta_B$, i.e. $\Delta\theta_B \sim \frac{\gamma_B|B|}{D_{gs}}$, indicating that the high angle sensitivity arises from the large zero-field splitting (D_{gs}). Second, the hyperfine interaction is the dominating term in the nuclear spin Hamiltonian, which directly affects its entanglement with the electron spin and therefore the spin-echo signal.

We also demonstrated a method to distinguish and characterize anisotropic noise in the XZ plane (i.e. δB_x and δB_z) based on the asymmetric angle dependence of coherence time. By further rotating the bias field in the XY plane (perpendicular to the NV axis), we could obtain information along all directions, which can help locate noise sources at the nanoscale. Moreover, we showed that the anisotropic component of the noise can be maximally decoupled by applying a bias field at the optimal angle, which may allow a great improvement of the NV spin coherence.

METHODS

Diamond sample

The diamond sample was an electronic-grade CVD diamond (Element Six), with a natural abundance (1.1%) of ^{13}C impurity spins. Negatively-charged NV centers were created by ion implantation (18 keV) followed by vacuum annealing at 800 °C for 2 h. NV experiments were performed on a home-built confocal laser scanning microscope. A 532 nm green laser was used to initialize the NV spin to the $m_S = 0$ state and generate spin-dependent photoluminescence for optical readout.

Spin dynamics simulation

The simulation of NV spin-echo decay was done using the QuTip (Quantum Toolbox in Python) software[58,59]. To simulate the coupling with the anisotropic magnetic noise, collapse operators were defined, and the time evolution was governed by the Lindblad master equation. More details are provided in Supplementary Note 4.

DATA AVAILABILITY

The data generated and analyzed during this study are available from the authors upon reasonable request.

CODE AVAILABILITY

The code used for simulation presented in this study is available from the authors upon reasonable request.

Received: 7 October 2020; Accepted: 17 December 2020;
Published online: 19 February 2021

REFERENCES

1. Budker, D. & Romalis, M. Optical magnetometry. *Nat. Phys.* **3**, 227–234 (2007).
2. Taylor, J. et al. High-sensitivity diamond magnetometer with nanoscale resolution. *Nat. Phys.* **4**, 810–816 (2008).
3. Degen, C. L., Reinhard, F. & Cappellaro, P. Quantum sensing. *Rev. Mod. Phys.* **89**, 1611.02427 (2017).
4. Dutt, M. G. et al. Quantum register based on individual electronic and nuclear spin qubits in diamond. *Science* **316**, 1312–1316 (2007).
5. Jiang, L. et al. Repetitive readout of a single electronic spin via quantum logic with nuclear spin ancillae. *Science* **326**, 267–272 (2009).
6. Zaiser, S. et al. Enhancing quantum sensing sensitivity by a quantum memory. *Nat. Commun.* **7**, 12279 (2016).
7. Maurer, P. C. et al. Room-temperature quantum bit memory exceeding one second. *Science* **336**, 1283–1286 (2012).
8. Rosskopf, T., Zopes, J., Boss, J. M. & Degen, C. L. A quantum spectrum analyzer enhanced by a nuclear spin memory. *npj Quantum Inf.* **3**, 1–7 (2017).
9. Dür, W., Skotiniotis, M., Froewis, F. & Kraus, B. Improved quantum metrology using quantum error correction. *Phys. Rev. Lett.* **112**, 080801 (2014).
10. Arrad, G., Vinkler, Y., Aharonov, D. & Retzker, A. Increasing sensing resolution with error correction. *Phys. Rev. Lett.* **112**, 150801 (2014).
11. Kessler, E. M., Lovchinsky, I., Sushkov, A. O. & Lukin, M. D. Quantum error correction for metrology. *Phys. Rev. Lett.* **112**, 150802 (2014).
12. Taminiau, T. H., Cramer, J., van der Sar, T., Dobrovitski, V. V. & Hanson, R. Universal control and error correction in multi-qubit spin registers in diamond. *Nat. Nanotechnol.* **9**, 171 (2014).

13. Hirose, M. & Cappellaro, P. Coherent feedback control of a single qubit in diamond. *Nature* **532**, 77–80 (2016).
14. Unden, T. et al. Quantum metrology enhanced by repetitive quantum error correction. *Phys. Rev. Lett.* **116**, 230502 (2016).
15. Schirhagl, R., Chang, K., Loretz, M. & Degen, C. L. Nitrogen-vacancy centers in diamond: nanoscale sensors for physics and biology. *Ann. Rev. Phys. Chem.* **65**, 83–105 (2014).
16. Casola, F., van der Sar, T. & Yacoby, A. Probing condensed matter physics with magnetometry based on nitrogen-vacancy centres in diamond. *Nat. Rev. Mater.* **3**, 1–13 (2018).
17. Bucher, D. B. et al. Quantum diamond spectrometer for nanoscale nmr and esr spectroscopy. *Nat. Protoc.* **14**, 2707–2747 (2019).
18. Maze, J. R. et al. Nanoscale magnetic sensing with an individual electronic spin in diamond. *Nature* **455**, 644–647 (2008).
19. Mamin, H. et al. Nanoscale nuclear magnetic resonance with a nitrogen-vacancy spin sensor. *Science* **339**, 557–560 (2013).
20. Hong, S. et al. Nanoscale magnetometry with nv centers in diamond. *MRS Bull.* **38**, 155–161 (2013).
21. Dolde, F. et al. Electric-field sensing using single diamond spins. *Nat. Phys.* **7**, 459–463 (2011).
22. Michl, J. et al. Robust and accurate electric field sensing with solid state spin ensembles. *Nano Lett.* **19**, 4904–4910 (2019).
23. Mittiga, T. et al. Imaging the local charge environment of nitrogen-vacancy centers in diamond. *Phys. Rev. Lett.* **121**, 246402 (2018).
24. Iwasaki, T. et al. Direct nanoscale sensing of the internal electric field in operating semiconductor devices using single electron spins. *ACS Nano* **11**, 1238–1245 (2017).
25. Block, M. et al. Optically enhanced electric field sensing using nitrogen-vacancy ensembles. Preprint at https://arxiv.org/abs/2004.02886 (2020).
26. Li, R. et al. Nanoscale electrometry based on a magnetic-field-resistant spin sensor. *Phys. Rev. Lett.* **124**, 247701 (2020).
27. Yang, B. et al. Vector electrometry in a wide-gap-semiconductor device using a spin-ensemble quantum sensor. *Phys. Rev. Appl.* **14**, 044049 (2020).
28. Barson, M. et al. Nanoscale vector electric field imaging using a single electron spin. Preprint at https://arxiv.org/abs/2011.12019 (2020).
29. Kucsko, G. et al. Nanometre-scale thermometry in a living cell. *Nature* **500**, 54–58 (2013).
30. Neumann, P. et al. High-precision nanoscale temperature sensing using single defects in diamond. *Nano Lett.* **13**, 2738–2742 (2013).
31. Toyli, D. M., Charles, F., Christle, D. J., Dobrovitski, V. V. & Awschalom, D. D. Fluorescence thermometry enhanced by the quantum coherence of single spins in diamond. *Proc. Natl. Acad. Sci. USA* **110**, 8417–8421 (2013).
32. Choi, J. et al. Probing and manipulating embryogenesis via nanoscale thermometry and temperature control. *Proc. Natl. Acad. Sci. USA*. https://www.pnas.org/content/early/2020/06/12/1922730117.full.pdf (2020).
33. Doherty, M. W. et al. Electronic properties and metrology applications of the diamond nv- center under pressure. *Phys. Rev. Lett.* **112**, 047601 (2014).
34. Ivády, V., Simon, T., Maze, J. R., Abrikosov, I. & Gali, A. Pressure and temperature dependence of the zero-field splitting in the ground state of nv centers in diamond: a first-principles study. *Phys. Rev. B* **90**, 235205 (2014).
35. Kehayias, P. et al. Imaging crystal stress in diamond using ensembles of nitrogen-vacancy centers. *Phys. Rev. B* **100**, 174103 (2019).
36. Gali, A. Hyperfine tensors of nitrogen-vacancy center in diamond from ab initio calculations. https://arxiv.org/pdf/0905.1169.pdf (2009).
37. Felton, S. et al. Hyperfine interaction in the ground state of the negatively charged nitrogen vacancy center in diamond. *Phys. Rev. B* **79**, 075203 (2009).
38. Smeltzer, B., McIntyre, J. & Childress, L. Robust control of individual nuclear spins in diamond. *Phys. Rev. A* **80**, 050302 (2009).
39. Rowan, L. G., Hahn, E. L. & Mims, W. B. Electron-spin-echo envelope modulation. *Phys. Rev.* **137**, A61–A71 (1965).
40. Childress, L. et al. Coherent dynamics of coupled electron and nuclear spin qubits in diamond. *Science* **314**, 281–285 (2006).
41. Maze, J. R., Taylor, J. M. & Lukin, M. D. Electron spin decoherence of single nitrogen-vacancy defects in diamond. *Phys. Rev. B - Condens. Matter and Mater. Phys.* **78**, 1–7 (2008).
42. Ohno, K. et al. Engineering shallow spins in diamond with nitrogen delta-doping. *Appl. Phys. Lett.* **101**. https://doi.org/10.1063/1.4748280 (2012).
43. Balasubramanian, G. et al. Ultralong spin coherence time in isotopically engineered diamond. *Nat. Mater.* **8**, 383–387 (2009).
44. Sangtawesin, S. et al. Origins of diamond surface noise probed by correlating single-spin measurements with surface spectroscopy. *Phys. Rev. X* **9**, 031052 (2019).
45. Siyushev, P. et al. Monolithic diamond optics for single photon detection. *Appl. Phys. Lett.* **97**, 241902 (2010).
46. Hadden, J. P. et al. Strongly enhanced photon collection from diamond defect centers under microfabricated integrated solid immersion lenses. *Appl. Phys. Lett.* **97**, 241901 (2010).
47. Castelletto, S. et al. Diamond-based structures to collect and guide light. *New J. Phys.* **13**, 025020 (2011).
48. Huang, T. Y. et al. A monolithic immersion metalens for imaging solid-state quantum emitters. *Nat. Commun.* **10**, 1–8 (2019).
49. Robledo, L. et al. High-fidelity projective read-out of a solid-state spin quantum register. *Nature* **477**, 574–578 (2011).
50. Babinec, T. M. et al. A diamond nanowire single-photon source. *Nat. Nanotechnol.* **5**, 195 (2010).
51. Hausmann, B. J. et al. Fabrication of diamond nanowires for quantum information processing applications. *Diam. Relat. Mater.* **19**, 621–629 (2010).
52. Maletinsky, P. et al. A robust scanning diamond sensor for nanoscale imaging with single nitrogen-vacancy centres. *Nat. Nanotechnol.* **7**, 320–324 (2012).
53. Appel, P. et al. Fabrication of all diamond scanning probes for nanoscale magnetometry. *Rev. Sci. Instrum.* **87**, 063703 (2016).
54. Zhou, T. X., Stöhr, R. J. & Yacoby, A. Scanning diamond NV center probes compatible with conventional AFM technology. *Appl. Phys. Lett.* **111**, 163106 (2017).
55. Bauch, E. et al. Ultralong dephasing times in solid-state spin ensembles via quantum control. *Phys. Rev. X* **8**, 031025 (2018).
56. Barry, J. F. et al. Sensitivity optimization for nv-diamond magnetometry. *Revi. Mod. Phys.* **92**, 015004 (2020).
57. Huillery, P. et al. Coherent microwave control of a nuclear spin ensemble at room temperature. Preprint at https://arxiv.org/abs/2005.13082 (2020).
58. Johansson, J. R., Nation, P. D. & Nori, F. QuTiP: an open-source Python framework for the dynamics of open quantum systems. *Comput. Phys. Commun.* **183**, 1760–1772 (2012).
59. Johansson, J. R., Nation, P. D. & Nori, F. QuTiP 2: a Python framework for the dynamics of open quantum systems. *Comput. Phys. Commun.* **184**, 1234–1240 (2013).

ACKNOWLEDGEMENTS

We gratefully thank Norman Y. Yao for valuable discussions and advice. Z.Q. also thanks Matthew Turner for diamond annealing assistance. This work was primarily supported by ARO Grant No. W911NF-17-1-0023. Fabrication of samples was supported by the U.S. Department of Energy, Basic Energy Sciences Office, Division of Materials Sciences and Engineering under award DE-SC0019300. A.Y. also acknowledges support from the STC Center for Integrated Quantum Materials, NSF Grant No. DMR-1231319, and the Aspen Center of Physics supported by NSF grant PHY-1607611.

AUTHOR CONTRIBUTIONS

A.Y. and Z.Q. conceived the project. Z.Q. performed the experiments, analyzed data, and produced figures. Z.Q., U.V., A.H. and A.Y. discussed the results and contributed to the writing of the manuscript. A.Y. supervised the project.

COMPETING INTERESTS

The authors declare no competing interests.

ADDITIONAL INFORMATION

Supplementary information The online version contains supplementary material available at https://doi.org/10.1038/s41534-021-00374-6.

Correspondence and requests for materials should be addressed to A.Y.

Reprints and permission information is available at http://www.nature.com/reprints

Publisher's note Springer Nature remains neutral with regard to jurisdictional claims in published maps and institutional affiliations.